The FEBS Journal

FEBS PRESS science publishing by scientists

Anions and citrate inhibit *Ls*AA9A, a lytic polysaccharide monooxygenase (LPMO)

Valerio Di Domenico[1,*], Yusuf Theibich[1], Søren Brander[2], Jean-Guy Berrin[3,4], Katja S. Johansen[2,†], Kristian E. H. Frandsen[1,5,‡] and Leila Lo Leggio[1]

1 Department of Chemistry, University of Copenhagen, Denmark
2 Department of Geosciences and Natural Resource Management, University of Copenhagen, Frederiksberg, Denmark
3 INRAE, Aix Marseille Univ., UMR 1163 Biodiversité et Biotechnologie Fongiques (BBF), Marseille, France
4 INRAE, Aix Marseille Univ., 3PE Platform, Marseille, France
5 Department of Plant & Environmental Sciences, University of Copenhagen, Frederiksberg, Denmark

Keywords
auxiliary activity; biomass; carbohydrate active enzymes; inhibitor; X-ray crystallography

Correspondence
L. Lo Leggio, Department of Chemistry, University of Copenhagen, Universitetsparken 5, 2100 Copenhagen Ø, Denmark
Tel: +45 35 32 02 95
E-mail: leila@chem.ku.dk
and
K. E. H. Frandsen, Department of Biotechnology and Biomedicine, Technical University of Denmark, Søltofts Plads, Building 221, 2800 Kgs. Lyngby, Denmark
Tel: +45 35 32 21 58
E-mail: kehfr@dtu.dk

Present address
*Structural Glycobiology Laboratory, Department of Structural and Molecular Biology; Molecular Biology Institute of Barcelona (IBMB), Spanish National Research Council (CSIC), Barcelona Science Park, Spain
†Department of Biochemistry, University of Cambridge, UK
‡Department of Biotechnology and Biomedicine, Technical University of Denmark, Kgs. Lyngby, Denmark

Valerio Di Domenico and Yusuf Theibich contributed equally to this article.

Lytic polysaccharide monooxygenases (LPMOs) are oxidative enzymes that break the glycosidic linkage in recalcitrant polysaccharides such as cellulose and chitin. The LPMO *Ls*AA9A (AA9 family lytic polysaccharide monooxygenase A) from the basidiomycete fungus *Lentinus similis* is biochemically and structurally well characterized, with crystallographic complexes with oligosaccharides having been obtained. Chloride ions from the crystallization solution are known to bind to the *Ls*AA9A–substrate complex in crystals at the copper equatorial coordinating position, where activation of the co-substrate oxygen species is expected. An investigation of the effect of high concentration salts on *Ls*AA9A activity showed that salts containing chloride and other halide anions, except for fluoride, had a clear inhibitory effect on the activity at concentrations > 100 mM, although chloride ions are known to increase the LPMO affinity for oligosaccharide binding. Surprisingly, *Ls*AA9A crystals can be transferred for short times to considerably different chemical environments, allowing crystallographic analysis at reduced chloride concentrations. Unfortunately, these washing steps do not eliminate the chloride binding at the copper equatorial coordinating position. Furthermore, we observed that citrate buffer, also present, bound under these changed chemical conditions at the copper active site. This interaction completely blocks access to the oligosaccharide substrate and is additionally supported here by citrate inhibition of *Ls*AA9A activities against azurine cross-linked hydroxyethylcellulose (AZCL-HEC), tamarind xyloglucan, and cellopentaose. The conclusions from our study indicate that citrate should be absolutely avoided in LPMO research, not only because of possible abstraction of copper ions from the LPMO active site but also because it might directly compete with binding of LPMOs to their target substrates.

Abbreviations
AA, auxiliary activities; ANSA, 3-amino-5-nitrosalicylic acid; AZCL-HEC, azurine cross-linked hydroxyethylcellulose; BSA, bovine serum albumin; CAZy, carbohydrate active enzymes; DNSA, 3,5-dinitrosalicylic acid; EPR, electron paramagnetic resonance; G3, cellotriose; G4, cellotetraose; G5, cellopentaose; G6, cellohexaose; HPAEC-PAD, high-performance anion-exchange chromatography with pulsed amperometric detection; LPMO, lytic polysaccharide monooxygenase; *Ls*AA9A, LPMO family AA9 isoform A from *Lentinus similis*; MES, (2-(N-morpholino)ethanesulfonic acid); PASC, phosphoric acid swollen cellulose; PEG, polyethylene glycol.

(Received 6 December 2024, revised 12 March 2025, accepted 9 May 2025)

doi:10.1111/febs.70138

Introduction

As climate change effects worsen, energy transition-oriented research has intensified. A considerable amount of attention has been received by enzymes for the production of transition biofuels by saccharification and subsequent fermentation of biomasses [1]. This intensive research has led to the discovery of novel carbohydrate-modifying enzymes, among which are lytic polysaccharide monooxygenases (LPMOs), extensively reviewed from different angles over the years (some examples in refs [2–8] covering structure–function relationships, mechanism, industrial applications, active site geometry and biological functions).

LPMOs are mono-nuclear copper enzymes dependent on a reductant and an oxygen species for cleavage of glycosidic bonds. LPMOs act in synergy with glycosyl hydrolases and other carbohydrate-active enzymes in the saccharification of complex polysaccharide-rich materials such as the lignified plant cell wall. As such, LPMOs are currently used in a commercial enzymatic cocktail in the full-scale production of lignocellulosic ethanol [3,4,9–11]. The catalytic action of LPMOs (Fig. 1A) was first defined as a monooxygenase reaction (with O_2 as co-substrate) but has since also been described as a peroxygenase [12] reaction (with H_2O_2 as co-substrate), which indeed predominates in recent literature. In the CAZy database [13], LPMOs are classified in 8 of the 17 auxiliary activity (AA) families defined currently. Among these, the AA9 family represents a large and well-established family of LPMOs, primarily active on cellulosic substrates and other polymers of β-1,4-linked pyranosides, though it also includes unusual members which are not LPMOs as they lack the copper binding motif [14].

The AA9 isoform A from *Lentinus similis* (*Ls*AA9A) has been structurally, biochemically, and spectroscopically characterized during the past few years [15–22]. These studies include the interactions with oligosaccharide ligands, co-substrates, and inhibitors, photoreduction of the active site metal, and a neutron crystallography structure. Due to the wealth of data available, this LPMO has also been the subject of computational mechanistic investigations [23,24] and as a model for the calculation of EPR (electron paramagnetic resonance) parameters [25]. *Ls*AA9A is active against many substrates such as cellulose, xyloglucans, mixed-linked β-glucans, glucomannans, isolated xylans, and oligosaccharides, and its primary oxidized products are at the C4 position [16]. A recent study [26] established that the breaking of the glycosidic linkage by *Ls*AA9A is dependent on H_2O_2, but the production of oxidized products is dependent on the presence of O_2. Unless the reaction conditions are very well controlled, H_2O_2 is produced in many common LPMO reaction mixtures [27], and exogenous addition is not necessary.

From a structural viewpoint, *Ls*AA9A shows the typical two-sheets immunoglobulin-like β-sandwich fold common to every LPMO structurally characterized so far (Fig. 1). The copper ion, located on top of this two-sheets fold (Fig. 1B), is responsible for its oxidative cleavage function and is coordinated by the characteristic histidine brace motif present in each characterized LPMO [28]. This motif is formed by the N-terminal histidine (found in a N-ε methylated form in natively expressed fungal LPMOs due to post-translation modification [29]), and a second histidine (His-78 in *Ls*AA9A). Furthermore, a tyrosine is often present and critically involved in AA9 LPMO activity (Tyr-164 in *Ls*AA9A, Fig. 1B), as shown even in some of the earliest mutational studies [30].

The AA9 LPMO substrate binding site [15–17] can be described as a rather flat and accessible surface, where cellooligosaccharides can bind to in some cases, as *Ls*AA9A and others [31,32] (Fig. 1). Cellohexaose (G6), cellopentaose (G5), cellotetraose (G4) and cellotriose (G3) bind to the active site at subsites −4 to +2, −3 to +2, −2 to +2, and −1 to +2, respectively. The sugar at the +1 subsite directly interacts with the N-terminal histidine. Tyr-203, a highly conserved residue in the LC loop (a loop in the C-terminal region) of most AA9 LPMOs, makes stacking interactions with the glucosyl units at subsite −3, in the case of G6 and G5 (Fig. 1B). Residues from the L2 and L3 loops contribute a number of hydrogen bond interactions with the substrate [4]. When *Ls*AA9A is in a Cu(II) form, the copper ion coordinates two water molecules,

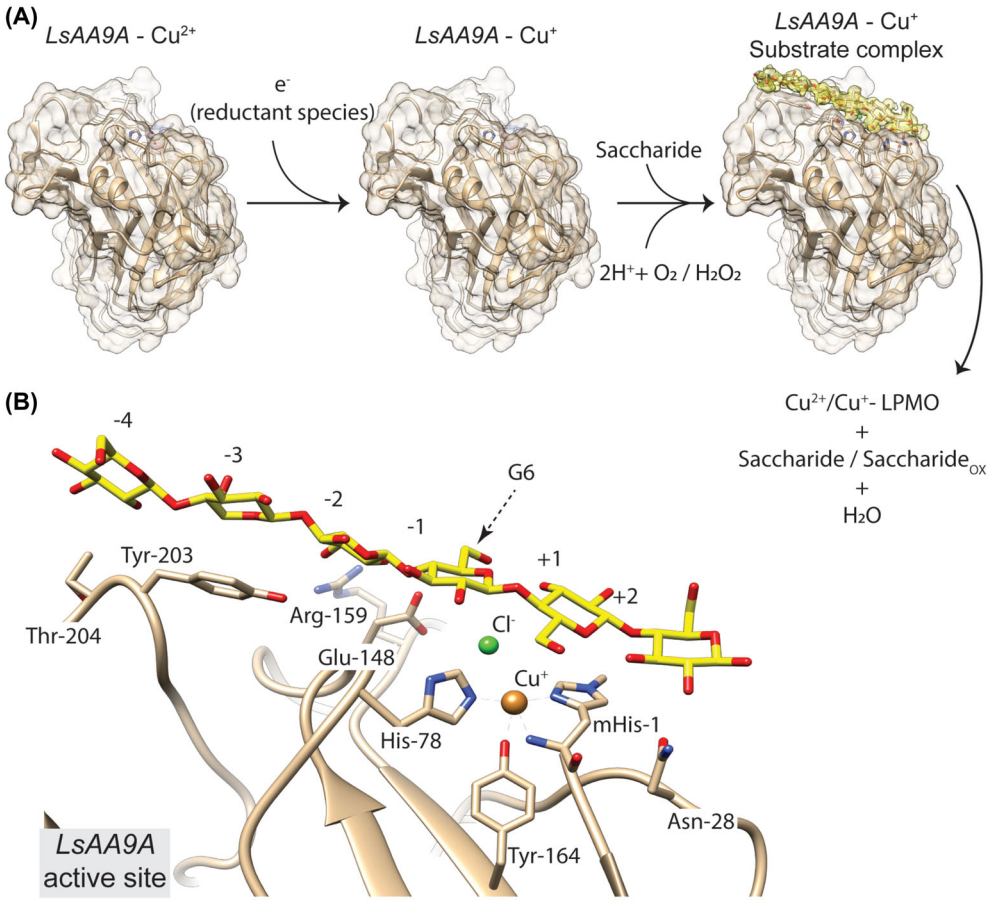

Fig. 1. Overall structure and reaction scheme of *Ls*AA9A. (A) Overall structure of *Ls*AA9A (PDB code 5ACG) (ribbon diagram) and reaction scheme for its peroxygenase activity on cellooligosaccharides; (B) Close-up visualization of the *Ls*AA9A Cu^+ (PDB code 5ACH) active site with bound cellohexaose (G6) moiety, with subsite numbering indicated. The N-terminal methylated histidine, histidine 78, and tyrosine 164 forming the active site are shown. The exogenous Cl^- ion, presumed to mimic the oxygen species during the LPMO saccharide cleavage, is shown. Figures were generated using UCSF ChimeraX [51].

one axial and one equatorial. Upon substrate binding, the axial water is displaced while the equatorial water is the presumed site of attack by the activated oxygen species. In crystallographic studies of *Ls*AA9A, the latter is, however, replaced by a chloride ion from the usual crystallization conditions (> 3 M NaCl) [15,16]. Though no longer in metal coordination distance, this exogenous chloride ion remains near the active site on reduction of the copper from Cu(II) (distance to Cl^-: 2.3 Å) to Cu(I) (distance to Cl^-: 3.9 Å) [20] and thus was presumed, at the high concentration in the crystal, to sterically hinder any crystallographic study of the putative oxygen/peroxide species that lead to completion of the oxidative cleavage.

In order to evaluate the importance of removing the chloride ion to observe the LPMO reaction in the crystals, we first evaluated the effect of various salts for the LPMO reaction and clearly saw that the effect at salt concentrations > 250 mM could severely reduce activity (typically 3.5 M NaCl are in our standard crystallization conditions). We thus devised protocols to transfer crystals to low chloride conditions. Surprisingly, in structures from these conditions, we observed previously unseen clear binding of the citrate buffer to the active site copper, where it would compete with binding of oligosaccharides in the crystals. This prompted us to evaluate – and indeed demonstrate– the potentially inhibitory effect of citrate on the *Ls*AA9A LPMO reaction.

For the crystallographic studies, we used the *Ls*AA9A recombinant enzyme expressed in *Aspergillus oryzae* that retains native posttranslational modifications [15]. However, it has been suggested that these preparations were contaminated by glycoside hydrolases [26]. Thus, for the biochemical studies, we primarily used an enzyme expressed in *Escherichia coli* (non-glycosylated

and devoid of His-tag) [33] (all experiments in main manuscript and Figs S3 and S4) with a few additional experiments (Figs S1 and S2) carried out with a His-tagged enzyme expressed in *Pichia pastoris* and purified as described previously [34].

Results

Chloride ions inhibit *Ls*AA9A activity

Given that chloride ions bind to the equatorial position of *Ls*AA9A when oligosaccharides bind to the active site in the crystal and remain in the vicinity even after copper reduction, we have assumed they would interfere with the LPMO reaction at the high concentrations used in crystallization, preventing the study of the reaction in the crystal. We were thus interested in investigating the effect of salts often present in high concentrations in crystallization mixtures on the *Ls*AA9A reaction. To assay the LPMO reaction, we initially used a chromogenic cellulosic substrate (AZCL-HEC) with cysteine (Cys) as reductant (as used for example in ref. [18]). Since *Ls*AA9A is a C4 cleaving LPMO, the 3,5-dinitrosalicylic acid (DNSA) assay detecting reducing sugars released from polysaccharides could also be used, with ascorbate (Asc) as reductant, as for example in ref. [35]. These simple assays are not adequate for mechanistic investigations but have been widely used for screening [36–38]. We chose not to add H_2O_2, though it is now known to be necessary for *Ls*AA9A activity, but rather relied on *in situ* production, not to further complicate the analysis by side reactions of excess H_2O_2 or rapid enzyme inactivation.

We detected clear inhibition of *Ls*AA9A by NaCl (Fig. 2A) in the azurine cross-linked hydroxyethylcellulose (AZCL-HEC) assay with Cys as reductant, confirmed in a time course over 2 h (Fig. 3A, Cys as reductant with 250 mM NaCl). Inhibition was confirmed using Asc as reductant in the same assay (Fig. 2B) and in a reducing end sugar assay using tamarind xyloglucan as substrate (dose response in Fig. 2C and time course in Fig. 3B).

The inhibitory activity can be ascribed to the chloride ions, as activity assays with xyloglucan comparing the standard LPMO reaction in the presence and absence of different salts indicate clearly that chloride and not sodium is responsible for inhibition (Fig. 2D). All group I chloride salts were similarly inhibitory. Sodium sulfate had little effect, excluding that the inhibition may result from the cation in the salt. Other halogens sodium salts were tested to see if the effect was unique to chloride.

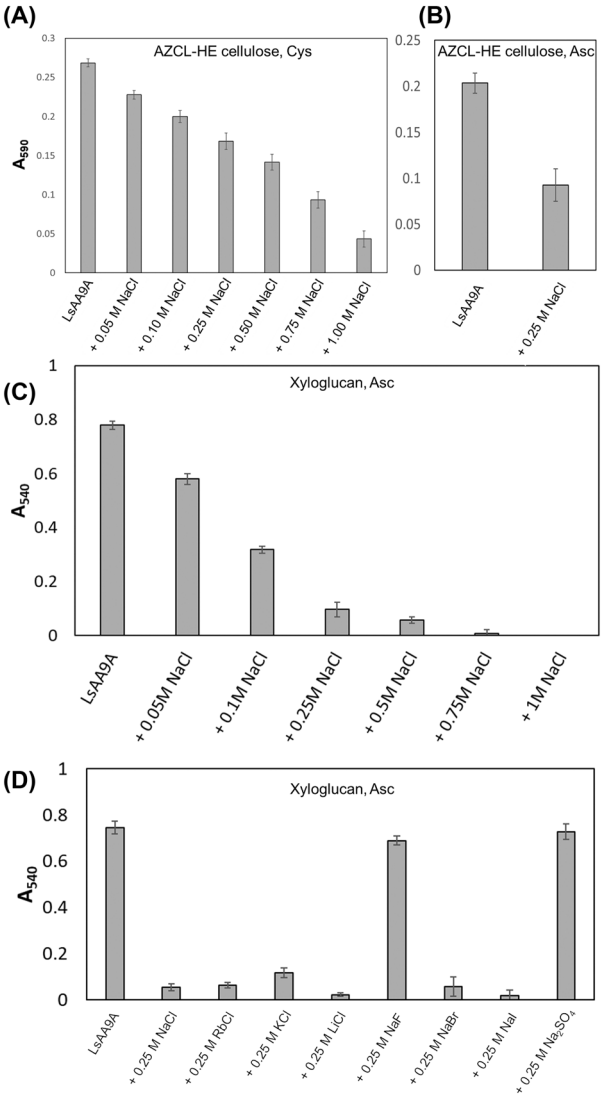

Fig. 2. Effect of NaCl and other salts on the activity of *Ls*AA9A. (A) The relative activity of *Ls*AA9A (5 μM) was evaluated using cysteine (Cys) as reducing agent (1 mM) and azurine cross-linked hydroxyethylcellulose (AZCL-HEC, 0.1% w/v) as substrate. Reactions were conducted in Na acetate buffer (100 mM, pH 5.5) for 2 h at 40 °C at 1000 rpm with increasing concentration of added NaCl and quenched by high pH. (B) The relative activity of *Ls*AA9A (5 μM) was evaluated in the same assay as in (A) but with ascorbic acid (Asc) as reducing agent (1 mM) in the presence or absence of 0.25 M NaCl. (C) The relative activity of *Ls*AA9A (5 μM) was evaluated with xyloglucan (0.25% w/v) as substrate with the DNSA (3,5-dinitrosalicylic acid) assay. Reactions were conducted in Na acetate buffer (100 mM, pH 5.5) for 1 h at 40 °C and 1000 rpm with increasing concentrations of added NaCl. (D) The relative activity of *Ls*AA9A (5 μM) was evaluated as in (C) in the presence of different salts. Errors bars represent standard deviations of triplicates, the A_{590} and A_{540} reported are after subtraction of appropriate blanks and corrected to a path length of 1 cm.

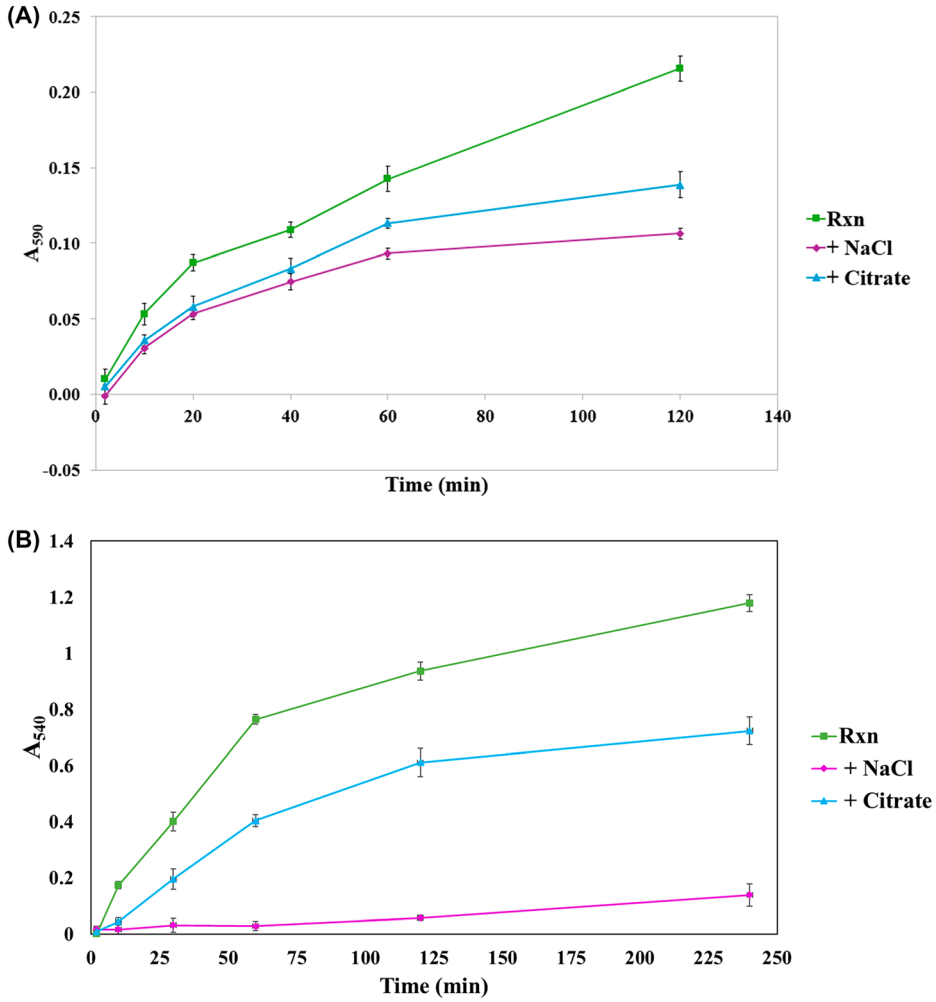

Fig. 3. Time courses of the activity of *Ls*AA9A. (A) *Ls*AA9A (5 μM) activity was measured using cysteine (Cys) as reducing agent (1 mM) and azurine cross-linked hydroxyethylcellulose (AZCL-HEC, 0.1% w/v) as substrate. Individual reactions were conducted in Na acetate buffer (100 mM, pH 5.5) for up to 2 h at 40 °C at 1000 rpm and quenched with high pH at each time point. The error bars represent the standard deviation for duplicates (inhibited reactions) or quadruplicates, and the A_{590} reported is after subtraction of appropriate blanks and corrected to a path length of 1 cm. The effect of 250 mM NaCl and 25 mM citrate are shown. (B) *Ls*AA9A (5 μM) activity was measured using ascorbate (Asc) as reducing agent (1 mM) and tamarind xyloglucan (0.25% w/v) as substrate. Individual reactions were conducted in Na acetate buffer (100 mM, pH 5.5) for up to 4 h at 40 °C at 1000 rpm. The error bars represent the standard deviation for triplicates, and the A_{540} reported is after subtraction of appropriate blanks and corrected to a path length of 1 cm. The effect of 250 mM NaCl and 25 mM citrate are shown.

Bromide and iodide salts were also inhibitory, while fluoride had little or no effect.

Qualitatively similar results were obtained with *Ls*AA9A produced in *P. pastoris* (Fig. S1a, in this case the reducing end assays were carried out with PASC instead).

Crystal transfer to reduce chloride content in *Ls*AA9A crystals reveals unexpected citrate bound at the active site copper

Clearly, the data above demonstrates that the LPMO reaction is severely inhibited by chloride ions at the concentrations used in crystallization. The presence of a chloride ion at or near the equatorial coordination in complexed crystal structures of *Ls*AA9A is a hindrance to the binding and correct identification of any activated oxygen species. EPR measurements also support the presence of this chloride ion upon substrate binding [15,16]. Thus, we devised a transfer strategy (see scheme in Fig. 4A,B) with the aim of washing out the excess chloride. Here, single crystals of *Ls*AA9A grown at the already reported crystallization conditions (between 3.2 and 3.8 M NaCl and 100 mM citrate buffer pH 3.5–4.0) are transferred to chloride-free

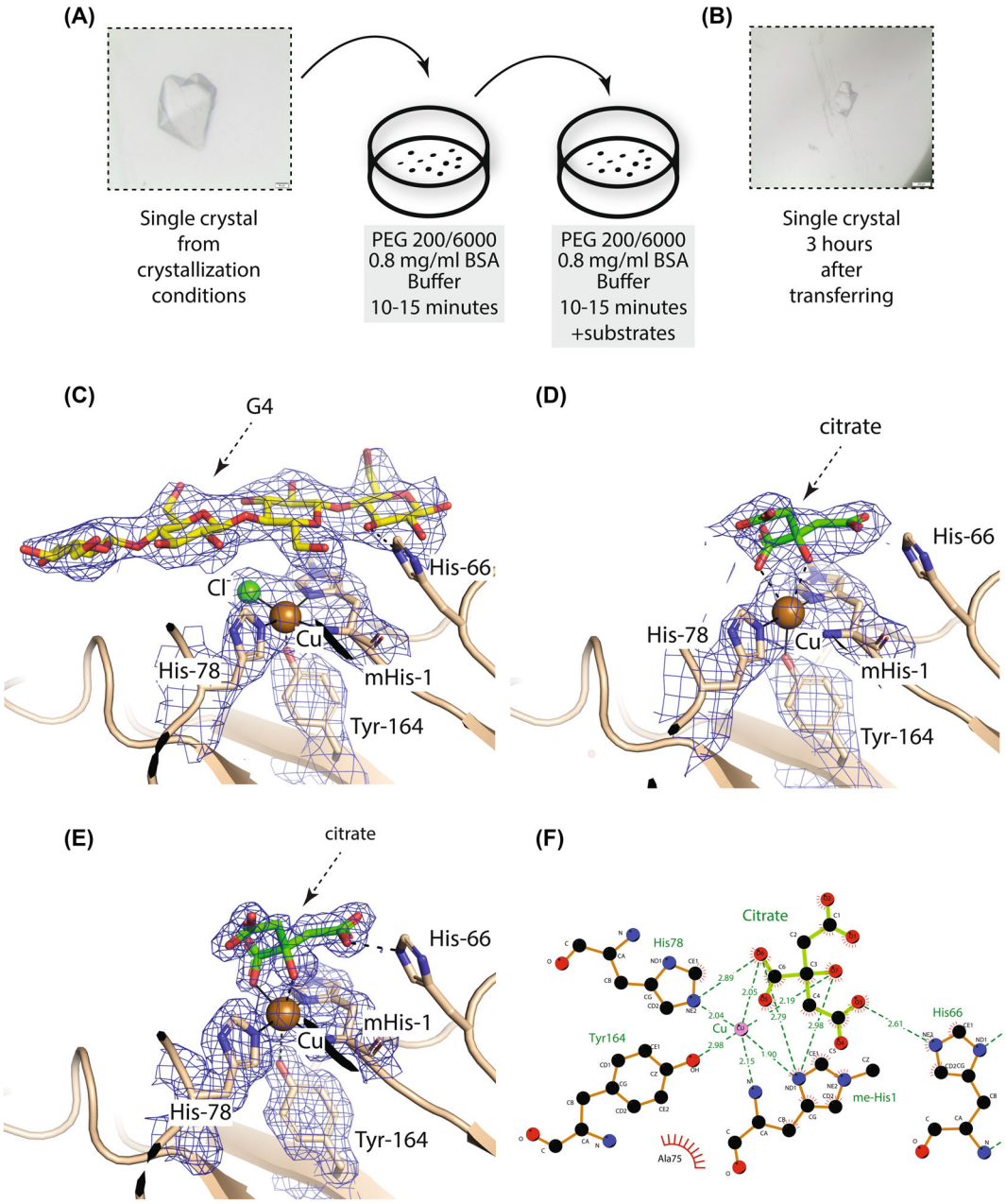

Fig. 4. Structures of *Ls*AA9A from crystals transferred to low chloride concentration conditions – (A) Schematic representation of the strategy for removing excess chloride from *Ls*AA9A crystals in conditions containing polyethylene glycol (PEG) and bovine serum albumin (BSA) (scale bar in crystal picture = 50 μm); (B) Picture of a transferred single crystal (taken after 3 h, scale bar = 200 μm); (C) transferred crystal structure with cellotetraose (G4) bound (*Ls*AA9A-G4 transferred); (D) transferred crystal structure with citrate bound (*Ls*AA9A-transferred); (E) transferred crystal structure with citrate bound, despite soaking with cellotetraose, known to bind at this concentration (*Ls*AA9A – transferred and G4 soaked); (F) schematic diagram for citrate binding. Figures were generated using PYMOL v. 2.6.2 (Schrödinger Inc. LLC, New York, NY, USA) and LIGPLOT+ v. 2.2 (EMBL-Hinxton, Cambridge, UK).

drops (disregarding any chloride from pH adjustment of buffers). We reasoned that precipitants frequently used for protein crystallization would decrease *Ls*AA9A solubility and help stabilize the crystals, even though they were not in the original mother liquor. The chosen transfer solutions are all PEG-based solutions in 100 mM citrate buffer pH 3.5, although many transfer trials have been performed also using a

Table 1. Crystallization, crystal handling, and crystallographic data.

	*Ls*AA9A-G4 (transferred)	*Ls*AA9A (transferred)	*Ls*AA9A (transferred and G4 soaked)
PDB entry	8S3L	9EQE	8S3F
Crystallization and crystal handling			
Crystallization conditions	3.8 M NaCl 0.1 M citrate buffer pH 3.5 in 96-wells MRC-2 plates with 70 µL of reservoirs and 0.3 µL drops	3.5 M NaCl 0.1 M citrate buffer pH 3.5 in 96-wells MRC-2 plates with 70 µL of reservoirs and 0.3 µL drops	3.7 M NaCl 0.1 M citrate buffer pH 3.5 in 96-wells MRC-2 plates with 70 µL of reservoirs and 0.3 µL drops
Transfer solution and soaking time	20% (w/v) PEG 6000, BSA 0.8 mg·mL^{-1}, 75 mM G4, 0.1 M citrate buffer pH 3.5 (10 min)	50% (w/v) PEG 6000, BSA 0.8 mg·mL^{-1}, 0.1 M citrate buffer pH 3.5 (3 h)	PEG 200 50% (w/v), BSA 0.8 mg·mL^{-1}, 0.1 M citrate buffer pH 3.5 (10 min)
Second transfer solution and soaking time	20% (w/v) PEG 6000, BSA 0.8 mg·mL^{-1}, 75 mM G4, 0.1 M citrate buffer pH 3.5 (10 min)		PEG 200 50% (w/v), BSA 0.8 mg·mL^{-1}, 75 mM G4, 0.1 M citrate buffer pH 3.5 (10 min)
Data collection			
Beamline	BioMAX – Max IV	P11 – DESY	BioMAX – Max IV
Wavelength (Å)	0.976	1.805	0.976
No. of images	200	100	200
Oscillation/image (°)	0.1	0.2	0.1
Space group	$P4_132$	$P4_132$	$P4_132$
Cell dimensions			
a, *b*, *c* (Å)	126.72, 126.72, 126.72	125.61, 125.61, 125.61	123.90, 123.90, 123.90
α, β, γ (°)	90, 90, 90	90, 90, 90	90, 90, 90
Resolution (Å)[a]	73.16–2.60 (2.67–2.60)	50.00–2.70 (2.77–2.70)	71.65–1.76 (1.80–1.76)
R_{meas}	13.7% (51.1%)	7.7% (21.2%)	11.8% (55.7%)
$I/\sigma I$	8.08 (2.17)	15.52 (7.11)	8.41 (2.31)
Completeness (%)	92.7 (97.1)	97.5 (97.5)	98.2 (99.0)
Multiplicity	4.56 (4.60)	3.88 (3.64)	4.38 (4.47)
CC(1/2) (%)	99.3 (79.9)	99.4 (97.3)	99.5 (82.4)
Refinement			
Resolution (Å)	73.27–2.60 (2.67–2.60)	44.45–2.70 (2.77–2.70)	71.65–1.76 (1.80–1.76)
No. of reflections	9820 (722)	9049 (637)	30 762 (2225)
R_{factor}/R_{free} (%)	19.87/26.22 (35.8/37.0)	17.63/23.85 (41.1/45.2)	15.68/18.72 (25.8/29.9)
No. of atoms			
Protein (incl. Cu)	1838	1859	1849
Ligand/PEG/ion	47	33	53
Water	43	127	272
B-factors (Å^2)			
Protein (incl. Cu)	41.54	23.61	18.07
Ligand/PEG/ion	46.69	60.47	40.76
Water	31.64	16.11	31.21
R.m.s. deviations			
Bond lengths (Å)	0.120	0.0565	0.0747
Bond angles (°)	1.382	1.404	1.571

[a]Resolution range for the highest resolution shell is in parentheses.

10-fold lower concentration buffer pH 4.0 in order to avoid a disordered active site as His residues become protonated and can no longer interact with the metal, as reported in ref. [39]. Furthermore, as protein solubility is also affected by the protein concentration, we found that crystals were stabilized by the presence of *Ls*AA9A in solution in the transfer liquor. Surprisingly, this could be replaced by commercial BSA (bovine serum albumin) which showed a stabilizing effect even at concentrations around 1 mg·mL^{-1} (see Table 1) and was the method of choice. This allowed transfer of crystals to significantly different solutions than the mother liquor, though resulting sometimes in slight damage or dissolution, as shown in Fig. 4.

Several structures were determined from crystals transferred, according to the strategy above, into transfer solutions also containing G4 (cellotetraose). An example of which (2.6 Å maximum resolution,

with active site copper in a non-reduced Cu(II) state) is shown (first column in Table 1, Fig. 4C). Once the initial protein model was placed, the G4 substrate was clearly visible and could be easily modeled in the electron density map on top of the active site, already from the first round of restrained refinement. Despite the applied transfer procedure, chloride was still present and could be modeled in its usual equatorial position with respect to the copper ion active site (both when in a Cu(II) state and in an essential fully reduced Cu(I) state), as is usually the case for oligosaccharide complexes of *Ls*AA9A [15]. Water modeled at this position resulted in the appearance of positive density in the difference map and a very low B-factor (data not shown). Thus, we could conclude that the desired aim of removing the chloride from the active site had not been fully achieved. However, intriguingly, transferred crystals that had not been subsequently soaked with G4 showed clear binding of citrate (Fig. 4D, second column in Table 1), which has never been observed before for these crystallization conditions. Furthermore, in some of the crystals soaked with 75 mM G4, the binding of G4 is outcompeted, and only citrate is visible in the structure (Fig. 4E, third column in Table 1). In both of these structures, citrate was clearly visible in the electron density from the first round of refinement and could be completely modeled.

Citrate is within coordination distance of Cu (2.1–2.2 Å) through its hydroxyl and one oxygen of a carboxylate group, which is at 2.9 Å from $N_{\varepsilon 2}$ of His78 of the histidine brace. Another carboxylate group of citrate interacts directly with His66 through a hydrogen bond (~ 2.6 Å O3-$N_{\varepsilon 2}$ distance), while a water network connects the citrate also with Gln162 and His147 in the secondary coordination sphere of the copper, and Ser77 and Asn28, which interact with cellooligosaccharides in crystal complexes. A schematic diagram showing bonding and distances is reported in Fig. 4F.

Citrate inhibits the LPMO reaction on chromogenic and soluble substrates at concentrations often used in biological assays

Given the tight binding to the active site copper and competition with saccharide binding in the crystal, we wanted to investigate the possibility of citrate being an inhibitor. Inhibition of *Ls*AA9A was detected in the AZCL-HEC assay with Cys and Asc as reductants (Figs 5A,B and 3A for time course). Inhibition by citrate was confirmed using the DNSA reducing sugar assay and tamarind xyloglucan (Fig. 5C and time course in Fig. 3B).

Furthermore, an ascorbate oxidation assay [40] was carried out in the presence of citrate without added H_2O_2. Figure 5D shows that citrate inhibits free copper (no LPMO) oxidation of ascorbate, likely through its known copper chelating effects even at low concentration, but also that it inhibits to some extent the LPMO-mediated ascorbate oxidation, consistent with citrate binding at the LPMO His-brace. As previously shown, the presence of G5 fully inhibits the ascorbate oxidation, presumably by competing with ascorbate for binding to the active site. This is also shown in the presence of citrate. It has been previously shown that *Ls*AA9A degrades G5 in a stoichiometric reaction with H_2O_2. In such a reaction, citrate inhibition was also confirmed (Fig. 5E).

Discussion

The work described here was originally motivated by the presumed activity interference caused by chloride ions in the known *Ls*AA9A crystallization conditions, preventing studies of the reaction *in crystallo*. Previous EPR measurements confirmed that chloride binds to the active site Cu in solution when saccharide substrates are present [15]. Isothermal Titration Calorimetry measurements also showed that chloride specifically decreases the apparent K_d for cellohexaose [15] suggesting a cooperative binding of chloride and saccharides. In those reports, it was suggested that chloride ions could function as active oxygen species mimics. As a consequence, one might expect that high concentrations of chloride ions might inhibit the saccharide cleavage activity by competing for binding with H_2O_2. To our knowledge, however, this inhibition has not been previously reported, but is clearly shown here despite some variability depending on protein batch and assay method. Furthermore, we clearly establish that at high concentrations all halide ions tested, except fluoride, are inhibitory. This may be due to the smaller ionic radius of fluoride (~ 1.2 Å) compared to chloride (~ 1.7 Å), bromide (~ 1.8 Å) or iodide (~ 2.1 Å). Thus, halides should be avoided at high concentrations in LPMO (or at least *Ls*AA9A) work.

The crystal transfer approach used here to circumvent the problem for crystallographic studies was unsuccessful in removing fully chloride ions from the *Ls*AA9A-oligosaccharide crystalline complex, but was significant in two important ways. Firstly, it demonstrated that crystals can sometimes be moved to stabilizing solutions vastly different from their mother liquor, an approach that may be useful in other contexts. Secondly, it led us to identify citrate in the crystal and demonstrate its inhibitory action on *Ls*AA9A.

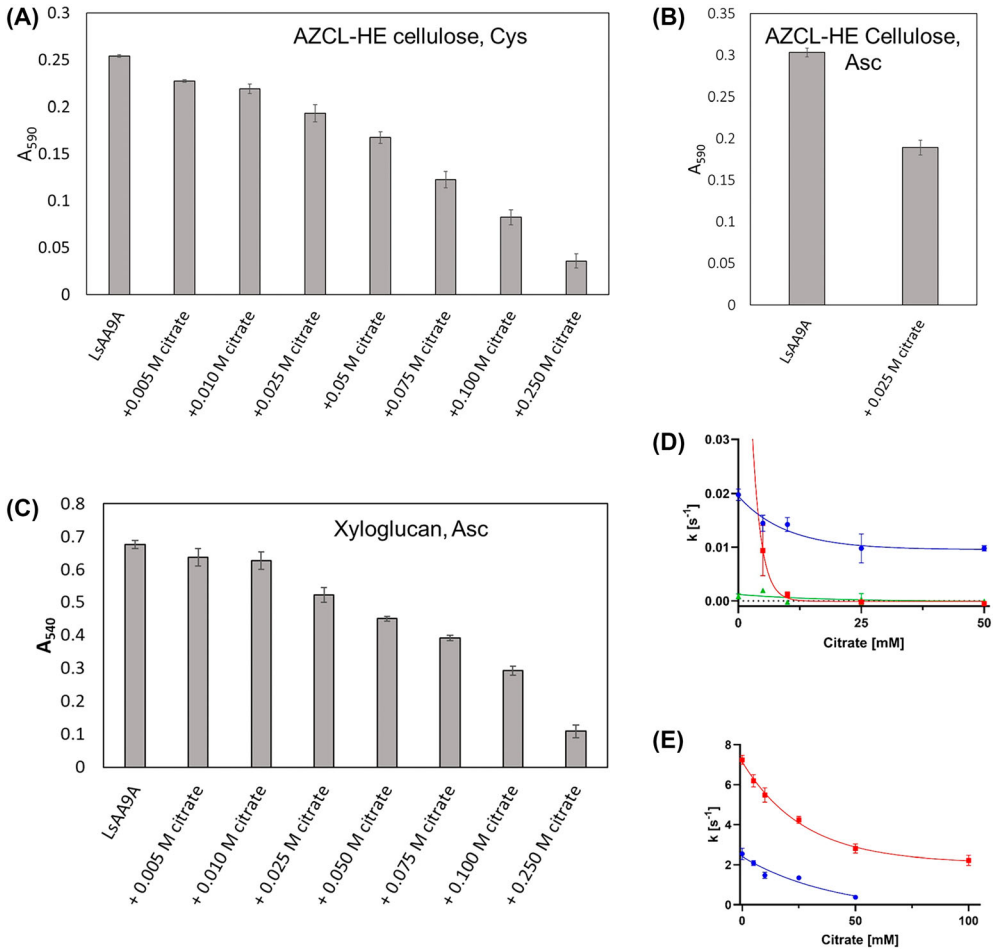

Fig. 5. Inhibitory effect of citrate on chromogenic and soluble substrates: (A) the activity of *Ls*AA9A was measured in the azurine cross-linked hydroxyethylcellulose (AZCL-HEC, 0.1% w/v) assay with cysteine (Cys, 1 mM) as reductant. Measurements were conducted in a Na acetate buffer (100 mM, pH 5.5) over a 2 h incubation at 40 °C and 1000 rpm with increasing concentration of citrate. (B) Inhibition was also observed under the same assay conditions as (A) with 1 mM ascorbic acid (Asc) as reductant and 25 mM citrate. (C) The activity of *Ls*AA9A (5 μM) on tamarind xyloglucan (0.25% w/v) was measured by the DNSA (3,5-dinitrosalicylic acid) assay using ascorbic acid (1 mM) as reducing agent with increasing concentrations of citrate, in Na acetate buffer (100 mM, pH 5.5) for 1 h at 40 °C and 1000 rpm. In a-c the A_{590} or A_{540} reported is after subtraction of appropriate blanks and corrected to a path length of 1 cm. (D) The inhibitory effect of citrate on *Ls*AA9A oxidation of ascorbate was measured by monitoring the specific absorption peak at 265 nm and calculating the reaction rates (Fig. S3). Samples are 20 mM MES buffer (2-(N-morpholino)ethanesulfonic acid), pH 6.0, 100 μM ascorbate and 0–50 mM citrate, pH 6.0 with catalysts 0.5 μM $CuCl_2$ (red), 0.5 μM Cu-*Ls*AA9A (blue) or 0.5 μM Cu-*Ls*AA9A with 100 μM cellopentaose (G5, green). Finally (E), the inhibitory effect of citrate on *Ls*AA9A H_2O_2-dependent cleavage of G5 was quantified by High-Performance Anion-Exchange Chromatography with Pulsed Amperometric Detection (HPAEC-PAD) and used to calculate the specific rates of cellotriose (G3, red) and cellobiose (G2, blue) product formation (Fig. S4). Samples are 20 mM MES, pH 6.0, 100 μM ascorbate, 100 μM G5, 0–50 mM citrate, 5 nM Cu-*Ls*AA9A and 40 μM H_2O_2. Reactions were stopped by addition of 0.1 M NaOH after 0–45 min incubation. In all panels the error bars represent the standard deviation for triplicates.

Previously, Breslmayr *et al.* [41] indicated citrate as a very poor buffer for *Nc*AA9C in the 2,6-dimethoxyphenol chromogenic assay. During the writing of the current manuscript, the same authors followed this up with a characterization of inhibition of the same enzyme by mono-, di-, and tri-carboxylic acids [42], where oxalic acid and citrate were found to be most inhibitory in colorimetric assays and PASC digestion as assessed by turbidity measurements. In their work, IC_{50} values were strongly dependent on the assays, but inhibition by citrate was also clearly demonstrated. At the same time, they also reported an increased oligosaccharide release from PASC in the presence of the carboxylic acid inhibitors, which

seemed counterintuitive. Thus, in our work here, we decided to focus on substrates other than PASC.

Our results show that citrate inhibits the action of *Ls*AA9A on the chromogenic substrate AZCL-HEC. Though citrate is not a potent inhibitor, it certainly will significantly affect the reaction at the concentrations where it is commonly used as a biological buffer and should hence be avoided, for example in inhibitor screening [18]. We additionally show inhibition of xyloglucan cleavage and a clear inhibition on the H_2O_2-driven G5 cleavage by *Ls*AA9A. Since we have determined many structures of *Ls*AA9A in the presence of 0.1 M citrate where the copper ion is present at full (or close to) occupancy, it seems unlikely that copper chelation by citrate can fully explain the inhibition. Furthermore, we observe inhibition also under very controlled conditions (Fig. 5E) where the fast reaction is not limited by *in situ* production of H_2O_2. Taken together, the crystallographic and biochemical evidence presented here suggests that citrate inhibits the *Ls*AA9A cleavage of glycosidic bonds at least partly by competitive inhibition.

Breslmayr *et al.* [42] computationally modeled the binding of various compounds and calculated binding energies, in agreement with oxalate and citrate being best binders. Here, we demonstrate for the first time the experimental interaction with citrate in a crystal structure of an LPMO, showing that, as in ref. [42] one carboxylate oxygen and hydroxyl group interact with the copper; however, in the crystal structure, it is the acetate rather than propionate group that interacts with copper. Furthermore, [42] reports severe distortion to the Cu-site geometry with a lengthened Cu-Tyr distance of ~ 3.4 Å, while in our structure (*Ls*AA9A – transferred and G4 soaked) it is 2.98 Å, only slightly longer than the average reported for Cu^{2+} saccharide-free structures of *Ls*AA9A (2.71 Å in ref. [20]) but still within the range reported for LPMOs (*e.g.*, 2.9–3.0 Å for the AA9 LPMO from *Thermoascus aurantiacus* [20]). The Cu-His1/His78/citrate distances are largely in agreement with computational models in ref. [42]. Electron density that might be ascribed to citrate near the active site of *Nc*AA9C was mentioned in ref. [32] but could not be modeled, and we are not aware of other crystal structures of AA9 LPMOs where it has been modeled in the active site, except for a recent structure of SmAA10 (PDB code 8RRY) where a disordered citrate is modeled only at one of the two molecules in the asymmetric unit (sandwiched between two protein molecules) [43]. The latter is unlikely to represent binding in solution.

The work presented here expands the very limited current knowledge of LPMO inhibition by small molecules, which in addition to carboxylic acids includes bioactive compounds from plants [18,44] cyanide, and phosphate inhibition [45], the latter reported in a very recent study published during the revision of this manuscript. Inhibition is relevant both for the use of LPMOs in bioreactors, their biological function, and their involvement in the pathogenesis of plants and animals, including humans [7]. Our anion inhibition study also suggested that alternative main precipitants should be found for the crystallization of *Ls*AA9A if the reaction is to be studied *in crystallo*. We have achieved this goal in a parallel study by identifying crystallization conditions for *Ls*AA9A produced in *E. coli* using ammonium sulphate as the main precipitant [20], which are promising for future crystallographic studies of the reaction.

Materials and methods

Chemicals

AZCL-HE-cellulose substrate, tamarind xyloglucan, G4, G5, and G6 substrates were purchased from Megazyme Ltd (Bray, Ireland). General chemicals were purchased from Sigma-Aldrich Merck KGaA (Darmstadt, Germany).

Protein production

For the crystallographic studies, we used the enzyme expressed in *Aspergillus oryzae* that retains native post-translational modifications, purified as in e.g., ref. [15]. The recombinant *Ls*AA9A expressed in fungi and used for crystallization was kindly provided by Novozymes A/S. Expression in *A. oryzae* and purification were carried out as in ref. [15]. *Ls*AA9A used for activity assays was primarily produced and purified from *E. coli* (periplasmic expression) as in ref. [33]. Few experiments were carried out with His-tagged *Ls*AA9A produced in *P. pastoris* and purified as described previously [34].

Prior to the AZCL-HEC and DNSA assay, a few mL of LPMO sample (8 $mg \cdot mL^{-1}$) was copper loaded by the addition of an equimolar amount of copper (II) acetate for 30 min at room temperature (stock solution 50 mM Cu(II) acetate) and subsequent dialysis against 300 mL of 20 mM NaOAc at pH 5.5 using a 3 mL Slide-A-Lyzer™ dialysis cassette [molecular weight cut-off (MWCO) of 10 kDa]. Prior to ascorbate oxidation and G5 cleavage assays, *Ls*AA9A was copper loaded with half a molar equivalent of $CuCl_2$.

Enzyme activity assays

AZCL-HEC assay

In the colorimetric AZCL-HEC substrate assay, 0.1% w/v AZCL-HEC, 5 μM Cu-*Ls*AA9A, 1 mM Ascorbate or

Cysteine, and 100 mM sodium acetate pH 5.5 of a total volume of 100 µL were incubated at 40 °C with constant shaking (1000 rpm) for 2 h, using a Thermo-shaker (Biosan 5TS-100). Reactions were quenched by adding 250 µL Tris-base (2% w/v, pH 10), and the soluble products were collected as the supernatant after centrifugation at 12 000 rpm (13 684 ***g***) for 10 min, using a Heraeus Megafuge 8R (with Microclick 24 × 2 microtube rotor from Thermo Fisher Scientific, Allerød, Denmark). The amount of released product was measured from the absorption of the blue dye at 590 nm as recommended by the manufacturer in microtiter plates using a spectrophotometer (PowerWave X; BioTek® Instruments Inc., Winooski, VT, USA). Controls where the reducing agent, substrate, or enzyme were omitted were carried out for each reaction set.

Ions inhibition experiments included the specified concentrations of added salt, without inclusion of ions included in normal pH adjustment of buffers. A time-course experiment was conducted using two inhibitors, NaCl and citrate (Fig. 3A). Citrate stock solutions were pH adjusted in each case to pH 5.5 using citric acid. For each time point, duplicates of three separate reactions were prepared in individual tubes (total volume 100 µL): (a) a control reaction containing 5 mM Cu-LsAA9A, 100 mM sodium acetate pH 5.5, 1 mM Ascorbate, and 0.1% AZCL-HEC, (b) a reaction with 250 mM NaCl under the same conditions as the control, and (c) a reaction with 25 mM citrate under the same conditions as the control. Reactions were quenched by adding 250 µL of Tris-base (2% w/v pH 10), following the same protocol used in previous experiments. Time points for stopping the reactions were 0, 10, 20, 40, 60, and 120 min.

Reducing end assay for PASC and xyloglucan

Xyloglucan substrate was prepared by dissolving 1 g of Tamarind xyloglucan (Megazyme P-XYGLN) in a 100 mL of 100 mM sodium acetate buffer (pH 5.5). The assay was performed with 0.25% w/v xyloglucan, 5 µM Cu-*Ls*AA9A, 1 mM Ascorbate or Cysteine, 100 mM sodium acetate pH 5.5 in a total reaction volume of 100 µL. Reactions were incubated at 40 °C with constant shaking (1000 rpm) for 1 h, using a thermo-shaker (Biosan TS-100; Biosan, Riga, Latvia).

The activity on xyloglucan was determined using the DNSA assay [36,46], which detects newly produced reducing ends of carbohydrates. A 50 µL of the reaction mixture was added to a 100 µL DNSA solution. The mixture was heated at 95 °C for 10 min to allow DNSA to react with reducing sugars. 100 µL of reaction mixtures were transferred to a 96-well microtiter plate and absorption at 540 nm (3-amino-5-nitrosalicylic acid ANSA product) was detected using a Powerwave X spectrophotometer.

A time-course experiment was conducted using two inhibitors, NaCl and citrate (Fig. 3B). Triplicates of the three separate reactions were prepared in a separate tube, each totaling 320 µL: (a) a control reaction containing 5 mM Cu-LsAA9A, 100 mM sodium acetate pH 5.5, 1 mM Ascorbate, and 0.25% xyloglucan, (b) a reaction with 250 mM NaCl under the same conditions as the control, and (c) a reaction with 25 mM citrate, under the same conditions as the control. Activity was detected using DNSA; at each time point, a 50 µL was taken from each tube, then following the same protocol used in previous experiments. Time points for stopping the reactions were 0, 10, 30, 60, 120, and 240 min.

For the assays in Fig. S1, PASC was prepared from Avicel (Fluka, PH-101). 0.2 g was wet in 0.6 mL H_2O and dissolved in 12 mL 86% phosphoric acid. After 1 h on ice with occasional stirring, 2 × 10 mL ice-cold water were added with occasional stirring; the cloudy precipitate was collected by centrifuging at 2000 ***g*** for 10 min at 4 °C. After discarding the supernatant, the precipitate was washed four times by adding 20 mL ice-cold water and removing it by centrifugation. 40 mL of ice-cold distilled water were added, and approximately 0.5 mL 2 M Na_2CO_3 was added to neutralize the residual phosphoric acid. After centrifugation (2000 ***g*** for 10 min at 4 °C), the supernatant was again removed, and 40 mL of ice-cold distilled water were added, and the pH was adjusted to 5.5. After repeating this last washing/pH adjustment step twice, a last centrifugation step was applied, after which the supernatant was discarded, the pH adjusted to 5.5, and the volume was added to 20 mL, obtaining a 1% w/v PASC stock solution for further use.

Activity on PASC was also determined using the DNSA assay. A mixture of 0.5% PASC, 5 µM Cu-*Ls*AA9A, 1 mM Ascorbate, and 100 mM sodium acetate buffer at pH 5.5 (total volume 100 µL) was incubated at 40 °C with shaking at 1000 rpm for 6 h. After incubation, the reaction was centrifuged for 10 min at 3000 rpm (855 ***g***), using a Heraeus Megafuge 8R with a Microclick 24 × 2 microtube rotor from Thermo Fisher Scientific. 50 µL of the supernatant was added to a 100 µL of DNSA solution. The mixture was heated at 95 °C for 10 min, and 100 µL of reaction mixes were transferred to a 96-well microtiter plate. Absorption was measured at 540 nm as for the xyloglucan activity assay. Appropriate controls were carried out similarly as for the AZCL-HEC assay, and the DNSA assay on xyloglucan. Anion inhibition experiments were similarly carried out.

Ascorbate oxidation assay

Ascorbate oxidation assays were carried out as a variation of the assays previously described [26]. All reagents were prepared in 20 mM MES, pH 6.0, treated with Chelex 100. The reagents were added in the following order: buffer, enzyme, G5, citrate, ascorbate, and H_2O_2. Samples containing 0.5 µM $CuCl_2$ or Cu-*Ls*AA9A, 0 or 100 µM G5, 0–50 mM citrate,

pH 6.0, and 100 μM ascorbate were prepared in a UV transparent microtiter plate and monitored in a Biotek Synergy H1 plate reader for 120 min. The oxidation of ascorbate was determined by the disappearance of the specific ascorbate band at 265 nm. Readouts from the inert reactions with G5 and *Ls*AA9A and the completely oxidized samples with $CuCl_2$ were used to deduce the specific absorption of 100 μM ascorbate (ΔAsc). The progress curves were fitted in the linear phase to give the slope, and the specific reaction rates were $k = -\text{slope}/(\Delta\text{Asc} \times 0.5\ \mu\text{M})$.

The effect of citrate on the kinetics of G5 cleavage

G5 degradation with H_2O_2 was performed in similar reactions, but with lower enzyme concentrations, and the injector module of the plate reader was used to start and quench the reactions. 12 samples for each citrate concentration were prepared, containing 5 nM Cu-*Ls*AA9A, 100 μM G5, 0–50 mM citrate, pH 6.0, and 100 μM ascorbate. Enzyme activity was initiated by injecting H_2O_2 to a concentration of 40 μM and quenched at preprogrammed time points by the addition of NaOH. G2 and G3 product formation was quantified by HPAEC-PAD and used to create an enzymatic progress curve. The slopes were fitted in the early phase, and the specific rates were calculated as $k = \text{slope}/(5\ \text{nM})$.

Crystallization, crystal transfer data collection, and structure determination

*Ls*AA9A expressed in *A. oryzae*, previously copper loaded as for AZCL-HE-cellulose and PASC assays above, was used for crystallization (23 $\text{mg}\cdot\text{mL}^{-1}$ in 20 mM NaOAc, pH 5.5). Crystallization conditions were similar as before and were all carried out in 96-well MRC-2 trays, with 0.3 μL drops and 70 μL of reservoirs. All crystallization experiments were performed at room temperature [15]. Exact crystallization conditions are given in Table 1. The *Ls*AA9A-G4 (transferred) crystal was firstly transferred and washed for 10 min in a 5 μL drop containing 20% (v/v) PEG 6000, 0.8 $\text{mg}\cdot\text{mL}^{-1}$ BSA, 100 mM Citric acid pH 3.5, in the presence of the substrate 75 mM G4. The crystal was then transferred once again into a new drop containing exactly the same composition for 10 more minutes. The second crystal (*Ls*AA9A – transferred) was washed for 3 h in the presence of 50% (v/v) PEG 6000, 0.8 $\text{mg}\cdot\text{mL}^{-1}$ BSA, 100 mM citric acid pH 3.5. For the *Ls*AA9A (transferred and G4 soaked) structure, the crystal was washed for 10 min in 50% (w/v) PEG 200, 0.8 $\text{mg}\cdot\text{mL}^{-1}$ BSA and 100 mMmM citric acid pH 3.5 and then transferred again for soaking in the same composition with the addition of 75 mM of the substrate G4 for 10 more minutes. Crystals were then plunged frozen in liquid nitrogen. For the first crystal ["*Ls*AA9A-G4 (transferred)"] a dataset was collected at BioMAX beamline, MAXIV. For the second crystal ("*Ls*AA9A (transferred)") an initial dataset (1800 images with 0.2° oscillation/image) were collected at beamline P11, DESY. Of this, a subset was processed in order to obtain a structure with the active site Cu(II) in its non-reduced form. For the third crystal ["*Ls*AA9A (transferred and G4 soaked)"] a dataset was collected at the BioMAX beamline, MAXIV.

Crystallographic data was processed and scaled using the XDS and XSCALE [47]. Structure determination was performed by importing R-free flags from a previously published *Ls*AA9A crystal structure (PDB entry: 5ACH) and initial maps were obtained through 10 rounds of rigid body refinement performed in Refmac [48] from the CCP4 suite [49]. Multiple rounds of manual inspections in *Coot* [50], followed by restrained refinements in Refmac, were performed until model validation was reached. All structures were refined isotropically for all atoms. Data collection and final refinement statistics are reported in Table 1.

Acknowledgements

We thank Novozymes A/S for providing purified *Ls*AA9A produced in *A. oryzae*; Cristina Hernández-Rollán and Morten Nørholm (Technical University of Denmark) for production of *Ls*AA9A in *E. coli* and Johan Ipsen (University of Copenhagen) for its purification. Leila Lo Leggio's group is part of ISBUC (Integrative Structural Biology at the University of Copenhagen). This study was funded by the Danish Council for Independent Research (grant No. 8021-00273B), the Novo Nordisk Foundation (Grant No. NNF17SA0027704 and NNF21OC0071799), Carlsberg Foundation (Internationalisation Postdoc Fellowship Grants CF16-0673 and CF17-0533), and Villum Foundation (Grant VIL50427). We thank the Danish Agency for Science, Technology, and Innovation for funding the instrument center DanScatt, supporting travel and sample shipping to synchrotrons. We acknowledge MAX IV Laboratory for time on Beamline Biomax under Proposal 20200120, 20220405, and 20240265. Research conducted at MAX IV, a Swedish national user facility, is supported by the Swedish Research council under contract 2018-07152, the Swedish Governmental Agency for Innovation Systems under contract 2018-04969, and Formas under contract 2019-02496. We acknowledge DESY (Hamburg, Germany), a member of the Helmholtz Association HGF, for the provision of experimental facilities at beamline P11. Beamline staff help at MAX IV and DESY are gratefully acknowledged.

Conflict of interest

The authors declare no conflict of interest.

Author contributions

VDD: Investigation, Methodology, Formal Analysis, Writing—review & editing, Visualization. KEHF: Conceptualization, Validation, Funding acquisition, Resources, Data curation, Writing—review & editing, Visualization, Supervision. YT: Methodology, Investigation, Validation, Writing—review & editing, Visualization, Supervision. SB: Methodology, Validation, Investigation, Formal Analysis, Writing—review & editing, Visualization. J-GB: Resources, Funding acquisition, Writing—review & editing, Supervision. KSJ: Conceptualization, Funding acquisition, Resources, Writing—review & editing, Supervision. LLL: Conceptualization; Funding acquisition; Formal Analysis, Visualization, Writing—original draft; Writing—review & editing, Supervision, Project Administration.

Peer review

The peer review history for this article is available at https://www.webofscience.com/api/gateway/wos/peer-review/10.1111/febs.70138.

Data availability statement

The structural data that support the findings of this study are openly available in Protein Data Bank at https://www.rcsb.org/. Accession numbers: PDB ID *Ls*AA9A-G4 (transferred): 8S3L; PDB ID *Ls*AA9A (transferred): 9EQE; PDB ID *Ls*AA9A (transferred and G4 soaked): 8S3F.

References

1 Pauly M & Keegstra K (2008) Cell-wall carbohydrates and their modification as a resource for biofuels. *Plant J* **54**, 559–568.

2 Johansen KS (2016) Discovery and industrial applications of lytic polysaccharide mono-oxygenases. *Biochem Soc Trans* **44**, 143–149.

3 Ipsen JØ, Hallas-Møller M, Brander S, Lo Leggio L & Johansen KS (2021) Lytic polysaccharide monooxygenases and other histidine-brace copper proteins: structure, oxygen activation and biotechnological applications. *Biochem Soc Trans* **49**, 531–540.

4 Frandsen KEH & Lo Leggio L (2016) Lytic polysaccharide monooxygenases – a crystallographer's view on a new class of biomass degrading enzymes. *IUCrJ* **3**, 448–467.

5 Bissaro B & Eijsink VGH (2023) Lytic polysaccharide monooxygenases: enzymes for controlled and site-specific Fenton-like chemistry. *Essays Biochem* **67**, 575–584.

6 Vu VV & Ngo ST (2018) Copper active site in polysaccharide monooxygenases. *Coord Chem Rev* **368**, 134–157.

7 Vandhana TM, Reyre J-L, Sushmaa D, Berrin J-G, Bissaro B & Madhuprakash J (2022) On the expansion of biological functions of lytic polysaccharide monooxygenases. *New Phytol* **233**, 2380–2396.

8 Munzone A, Eijsink VGH, Berrin J-G & Bissaro B (2024) Expanding the catalytic landscape of metalloenzymes with lytic polysaccharide monooxygenases. *Nat Rev Chem* **8**, 106–119.

9 Tandrup T, Frandsen KEH, Johansen KS, Berrin JG & Lo Leggio L (2018) Recent insights into lytic polysaccharide monooxygenases. *Biochem Soc Trans* **46**, 1431–1447.

10 Span EA & Marletta MA (2015) The framework of polysaccharide monooxygenase structure and chemistry. *Curr Opin Struct Biol* **35**, 93–99.

11 Eijsink VGH, Petrovic D, Forsberg Z, Mekasha S, Røhr ÅK, Várnai A, Bissaro B & Vaaje-Kolstad G (2019) On the functional characterization of lytic polysaccharide monooxygenases (LPMOs). *Biotechnol Biofuels* **12**, 58.

12 Bissaro B, Rohr AK, Muller G, Chylenski P, Skaugen M, Forsberg Z, Horn SJ, Vaaje-Kolstad G & Eijsink VGH (2017) Oxidative cleavage of polysaccharides by monocopper enzymes depends on H_2O_2. *Nat Chem Biol* **13**, 1123–1128.

13 Drula E, Garron ML, Dogan S, Lombard V, Henrissat B & Terrapon N (2022) The carbohydrate-active enzyme database: functions and literature. *Nucleic Acids Res* **50**, D571–D577.

14 Frandsen KE, Tovborg M, Jørgensen CI, Spodsberg N, Rosso M-N, Hemsworth GR, Garman EF, Grime GW, Poulsen J-CN & Batth TS (2019) Insights into an unusual auxiliary activity 9 family member lacking the histidine brace motif of lytic polysaccharide monooxygenases. *J Biol Chem* **294**, 17117–17130.

15 Frandsen KE, Simmons TJ, Dupree P, Poulsen JC, Hemsworth GR, Ciano L, Johnston EM, Tovborg M, Johansen KS, von Freiesleben P *et al.* (2016) The molecular basis of polysaccharide cleavage by lytic polysaccharide monooxygenases. *Nat Chem Biol* **12**, 298–303.

16 Simmons TJ, Frandsen KEH, Ciano L, Tryfona T, Lenfant N, Poulsen JC, Wilson LFL, Tandrup T, Tovborg M, Schnorr K *et al.* (2017) Structural and electronic determinants of lytic polysaccharide monooxygenase reactivity on polysaccharide substrates. *Nat Commun* **8**, 1064.

17 Tandrup T, Tryfona T, Frandsen KEH, Johansen KS, Dupree P & Lo Leggio L (2020) Oligosaccharide binding and thermostability of two related AA9 lytic

polysaccharide monooxygenases. *Biochemistry* **59**, 3347–3358.
18 Tokin R, Frandsen KEH, Ipsen JØ, Lo Leggio L, Poojary MM, Berrin J-G, Grisel S, Brander S, Jensen PE & Johansen KS (2021) Inhibition of lytic polysaccharide monooxygenase by natural plant extracts. *New Phytol* **232**, 1337–1349.
19 Banerjee S, Muderspach SJ, Tandrup T, Frandsen KEH, Singh RK, Ipsen JØ, Hernández-Rollán C, Nørholm MHH, Bjerrum MJ, Johansen KS *et al.* (2022) Protonation state of an important histidine from high resolution structures of lytic polysaccharide monooxygenases. *Biomolecules* **12**, 194.
20 Tandrup T, Muderspach SJ, Banerjee S, Santoni G, Ipsen JO, Hernandez-Rollan C, Norholm MHH, Johansen KS, Meilleur F & Lo Leggio L (2022) Changes in active-site geometry on X-ray photoreduction of a lytic polysaccharide monooxygenase active-site copper and saccharide binding. *IUCrJ* **9**, 666–681.
21 Tandrup T, Lo Leggio L & Meilleur F (2023) Joint X-ray/neutron structure of *Lentinus similis* AA9_A at room temperature. *Acta Crystallogr Sect F* **79**, 1–7.
22 Zhao J, Zhuo Y, Diaz DE, Shanmugam M, Telfer AJ, Lindley PJ, Kracher D, Hayashi T, Seibt LS, Hardy FJ *et al.* (2023) Mapping the initial stages of a protective pathway that enhances catalytic turnover by a lytic polysaccharide monooxygenase. *J Am Chem Soc* **145**, 20672–20682.
23 Wang B, Johnston EM, Li P, Shaik S, Davies GJ, Walton PH & Rovira C (2018) QM/MM studies into the H_2O_2-dependent activity of lytic polysaccharide monooxygenases: evidence for the formation of a caged hydroxyl radical intermediate. *ACS Catal* **8**, 1346–1351.
24 Hedegård ED & Ryde U (2017) Targeting the reactive intermediate in polysaccharide monooxygenases. *J Biol Inorg Chem* **22**, 1029–1037.
25 Theibich YA, Sauer SPA, Leggio LL & Hedegård ED (2021) Estimating the accuracy of calculated electron paramagnetic resonance hyperfine couplings for a lytic polysaccharide monooxygenase. *Comput Struct Biotechnol J* **19**, 555–567.
26 Brander S, Tokin R, Ipsen JØ, Jensen PE, Hernández-Rollán C, Nørholm MHH, Leggio LL, Dupree P & Johansen KS (2021) Scission of glucosidic bonds by a *Lentinus similis* lytic polysaccharide monooxygenases is strictly dependent on H_2O_2 while the oxidation of saccharide products depends on O2. *ACS Catal* **11**, 13848–13859.
27 Scott BR, Huang HZ, Frickman J, Halvorsen R & Johansen KS (2016) Catalase improves saccharification of lignocellulose by reducing lytic polysaccharide monooxygenase-associated enzyme inactivation. *Biotechnol Lett* **38**, 425–434.
28 Quinlan RJ, Sweeney MD, Lo Leggio L, Otten H, Poulsen J-CN, Johansen KS, Krogh KBRM, Jorgensen CI, Tovborg M, Anthonsen A *et al.* (2011) Insights into the oxidative degradation of cellulose by a copper metalloenzyme that exploits biomass components. *Proc Natl Acad Sci USA* **108**, 15079–15084.
29 Batth TS, Simonsen JL, Hernández-Rollán C, Brander S, Morth JP, Johansen KS, Nørholm MHH, Hoof JB & Olsen JV (2023) A seven-transmembrane methyltransferase catalysing N-terminal histidine methylation of lytic polysaccharide monooxygenases. *Nat Commun* **14**, 4202.
30 Harris PV, Welner D, McFarland KC, Re E, Navarro Poulsen JC, Brown K, Salbo R, Ding H, Vlasenko E, Merino S *et al.* (2010) Stimulation of lignocellulosic biomass hydrolysis by proteins of glycoside hydrolase family 61: structure and function of a large, enigmatic family. *Biochemistry* **49**, 3305–3316.
31 Bennati-Granier C, Garajova S, Champion C, Grisel S, Haon M, Zhou S, Fanuel M, Ropartz D, Rogniaux H, Gimbert I *et al.* (2015) Substrate specificity and regioselectivity of fungal AA9 lytic polysaccharide monooxygenases secreted by Podospora anserina. *Biotechnol Biofuels* **8**, 90.
32 Borisova AS, Isaksen T, Dimarogona M, Kognole AA, Mathiesen G, Várnai A, Røhr ÅK, Payne CM, Sørlie M, Sandgren M *et al.* (2015) Structural and functional characterization of a lytic polysaccharide monooxygenase with broad substrate specificity. *J Biol Chem* **290**, 22955–22969.
33 Hernández-Rollán C, Falkenberg KB, Rennig M, Bertelsen AB, Ipsen JØ, Brander S, Daley DO, Johansen KS & Nørholm MHH (2021) LyGo: a platform for rapid screening of lytic polysaccharide monooxygenase production. *ACS Synth Biol* **10**, 897–906.
34 Frandsen KEH, Haon M, Grisel S, Henrissat B, Lo Leggio L & Berrin J-G (2021) Identification of the molecular determinants driving the substrate specificity of fungal lytic polysaccharide monooxygenases (LPMOs). *J Biol Chem* **296**, 100086.
35 Martinez-D'Alto A, Yan X, Detomasi TC, Sayler RI, Thomas WC, Talbot NJ & Marletta MA (2023) Characterization of a unique polysaccharide monooxygenase from the plant pathogen Magnaporthe oryzae. *Proc Natl Acad Sci USA* **120**, e2215426120.
36 Navarro D, Couturier M, Damasceno da Silva GG, Berrin J-G, Rouau X, Asther M & Bignon C (2010) Automated assay for screening the enzymatic release of reducing sugars from micronized biomass. *Microb Cell Factories* **9**, 58.
37 Grandmontagne D, Navarro D, Neugnot-Roux V, Ladevèze S & Berrin J-G (2021) The secretomes of *Aspergillus japonicus* and *Aspergillus terreus* supplement

the Rovabio® enzyme cocktail for the degradation of soybean meal for animal feed. *J Fungi* **7**, 278.
38 Chabbert B, Habrant A, Herbaut M, Foulon L, Aguié-Béghin V, Garajova S, Grisel S, Bennati-Granier C, Gimbert-Herpoël I, Jamme F *et al.* (2017) Action of lytic polysaccharide monooxygenase on plant tissue is governed by cellular type. *Sci Rep* **7**, 17792.
39 Frandsen KEH, Poulsen J-CN, Tandrup T & Lo Leggio L (2017) Unliganded and substrate bound structures of the cellooligosaccharide active lytic polysaccharide monooxygenase LsAA9A at low pH. *Carbohydr Res* **448**, 187–190.
40 Brander S, Horvath I, Ipsen JØ, Peciulyte A, Olsson L, Hernández-Rollán C, Nørholm MHH, Mossin S, Leggio LL, Probst C *et al.* (2020) Biochemical evidence of both copper chelation and oxygenase activity at the histidine brace. *Sci Rep* **10**, 16369.
41 Breslmayr E, Hanžek M, Hanrahan A, Leitner C, Kittl R, Šantek B, Oostenbrink C & Ludwig R (2018) A fast and sensitive activity assay for lytic polysaccharide monooxygenase. *Biotechnol Biofuels* **11**, 79.
42 Breslmayr E, Poliak P, Požgajčić A, Schindler R, Kracher D, Oostenbrink C & Ludwig R (2022) Inhibition of the peroxygenase lytic polysaccharide monooxygenase by carboxylic acids and amino acids. *Antioxidants (Basel)* **11**, 1096.
43 Munzone A, Pujol M, Tamhankar A, Joseph C, Mazurenko I, Réglier M, Jannuzzi SAV, Royant A, Sicoli G, DeBeer S *et al.* (2024) Integrated experimental and theoretical investigation of copper active site properties of a lytic polysaccharide monooxygenase from *Serratia marcescens*. *Inorg Chem* **63**, 11063–11078.
44 Tokin R, Ipsen JØ, Poojary MM, Jensen PE, Olsson L & Johansen KS (2021) Inhibition of LPMOs by fermented persimmon juice. *Biomolecules* **11**, 1890.
45 Golten O, Schwaiger L, Forsberg Z, Hall KR, Stepnov AA, Emrich-Mills TZ, Ayuso-Fernández I, Sørlie M, Ludwig R, Røhr ÅK *et al.* (2025) Functional variation among LPMOs revealed by the inhibitory effects of cyanide and buffer ions. *FEBS Lett* **599**, 1317–1336.
46 Miller GL (1959) Use of dinitrosalicylic acid reagent for determination of reducing sugars. *Anal Chem* **31**, 426–428.
47 Kabsch W (2010) XDS. *Acta Crystallogr D Biol Crystallogr* **66**, 125–132.
48 Vagin AA, Steiner RA, Lebedev AA, Potterton L, McNicholas S, Long F & Murshudov GN (2004) REFMAC5 dictionary: organization of prior chemical knowledge and guidelines for its use. *Acta Crystallogr D Biol Crystallogr* **60**, 2184–2195.
49 Winn MD, Ballard CC, Cowtan KD, Dodson EJ, Emsley P, Evans PR, Keegan RM, Krissinel EB, Leslie AGW, McCoy A *et al.* (2011) Overview of the CCP4 suite and current developments. *Acta Crystallogr D Biol Crystallogr* **67**, 235–242.
50 Emsley P, Lohkamp B, Scott WG & Cowtan K (2010) Features and development of coot. *Acta Crystallogr D Biol Crystallogr* **66**, 486–501.
51 Meng EC, Goddard TD, Pettersen EF, Couch GS, Pearson ZJ, Morris JH & Ferrin TE (2023) UCSF ChimeraX: tools for structure building and analysis. *Protein Sci* **32**, e4792.

Supporting information

Additional supporting information may be found online in the Supporting Information section at the end of the article.

Fig. S1. Effect of NaCl and other salts on the activity of *Ls*AA9A recombinantly produced in *P. pastoris* (marked as LsAA9A_y).

Fig. S2. Inhibition by citrate on *Ls*AA9A (5 μM) recombinantly produced in *P. pastoris* (marked as LsAA9A_y).

Fig. S3. Ascorbate oxidation was measured by the reduction of the ascorbate-specific absorption band at 265 nm in the time span of 100 min.

Fig. S4. Cellopentaose degradation was measured as described in [26].